

Broadband spectral and emission geometry analysis of XB 1916–053 with *Chandra* and *NuSTAR*

Rahul Sharma ^{a,b}, , ^{*}

^a Inter-University Centre for Astronomy and Astrophysics (IUCAA), Ganeshkhind, Pune, 411007, Maharashtra, India

^b Raman Research Institute, C V Raman Avenue, Sadashivanagar, Bangalore, 560080, Karnataka, India

ARTICLE INFO

Dataset link: <https://heasarc.gsfc.nasa.gov/db-perl/W3Browse/w3browse.pl>

Keywords:

Accretion

Accretion disks

Techniques: spectroscopic

Stars: neutron

X-rays: binaries

X-rays: individual: XB 1916–053 (4U 1915-05)

ABSTRACT

We report results from a broad-band spectral analysis of the dipping neutron star low-mass X-ray binary XB 1916–053 using the *Chandra* and *Nuclear Spectroscopic Telescope Array (NuSTAR)* observation. The spectrum can be well described with a combination of emission from a multi-colour disk ($kT_{\text{in}} \sim 0.7$ keV), a single-temperature blackbody ($kT_{\text{BB}} \sim 1.4$ keV), and thermal Comptonization components ($\Gamma \sim 1.9$; $kT_{\text{e}} \sim 17$ keV), with the neutron star surface (or boundary layer) serving as the primary source of Comptonizing seed photons. The timing and spectral properties suggest that the source is in a soft state, albeit with a relatively high electron corona temperature. Additionally, absorption features were detected in the persistent spectrum from the highly ionized Si, S, Ar, Ca, Fe and a blend of highly ionized Fe $K\beta$ and Ni $K\alpha$ transitions. These features suggest the presence of a highly ionized atmosphere above the accretion disk during persistent intervals. During the dipping intervals, the line of sight is obscured by the outer disk structure or bulge, which is denser and less ionized.

1. Introduction

Low Mass X-ray Binaries (LMXBs) are celestial systems characterized by the presence of a compact object, either a neutron star (NS) or a black hole (BH), paired with a low-mass companion star with a mass typically $\lesssim 1$ solar mass (M_{\odot}) (for review see, e.g., Bahramian and Degenaar, 2023). In these binaries, the compact object draws material from its companion through accretion, leading to the emission of X-rays. The accretion rate is usually inferred from the position of the sources in their X-ray colour-colour diagrams or hardness-intensity diagrams (HIDs; Lewin and van der Klis, 2006). LMXBs exhibit distinctive patterns in these diagrams, and their luminosity spans a range of $0.001 - 0.5 L_{\text{Edd}}$ (van der Klis, 2006), where L_{Edd} is Eddington Luminosity. The low luminosity sources trace out an atoll-like shape, with the different branches referred to as the banana branch associated with a high inferred accretion rate and the island state corresponding to a low inferred accretion rate (Hasinger and van der Klis, 1989).

The X-ray emission from NS LMXBs consists of three primary components: disk blackbody emission originating from the accretion disk, a blackbody component from the NS surface or boundary layer and a Comptonization component arising from the scattering of soft X-rays in the surrounding corona (Done et al., 2007; Lin et al., 2007, 2009; Ar-

mas Padilla et al., 2017; Sharma et al., 2018). During the soft state of NS LMXBs, the emission is dominated by thermal components, with a weak Comptonized component characterized by low temperature and high optical depth (Bloser et al., 2000; Sakurai et al., 2012; Armas Padilla et al., 2017; Sharma et al., 2018, 2020a). In the hard state, the spectra are dominated by a hard Comptonized component exhibiting temperatures in the range of several tens of keV and low optical depths. The thermal components are observed at lower temperatures ($kT < 1$ keV) and significantly reduced luminosity levels (e.g., Sakurai et al., 2012; Zhang et al., 2016; Armas Padilla et al., 2017; Sharma et al., 2018).

Narrow absorption features from highly ionized Fe and other elements have been observed in several NS LMXBs (e.g., Sidoli et al., 2001; Díaz Trigo et al., 2006; Hyodo et al., 2009; Ponti et al., 2014, 2015; Raman et al., 2018; Sharma et al., 2018). These systems typically have high inclination angles, with many being classified as dippers (Boirin et al., 2004; Díaz Trigo et al., 2006; Díaz Trigo and Boirin, 2013). The highly ionized plasma giving rise to these features is hypothesized to originate within the atmosphere or wind of the accretion disk. These high-inclination sources also provide an opportunity to study the precise orbital evolution in LMXBs, where eclipses (Jain et al., 2017, 2022; Ponti et al., 2017; Iaria et al., 2018) or the periodic dips (Iaria et al., 2015, 2021; Gambino et al., 2016) can be used as the marker. Few sys-

* Corresponding author.

E-mail address: rahul1607kumar@gmail.com.

tems also show the signature of a triple system (Jain et al., 2017; Iaria et al., 2018, 2021).

1.1. XB 1916–053

XB 1916–053 (also known as 4U 1915-05) is an atoll NS LMXB system that was discovered with *Einstein Observatory* in 1977 (Becker et al., 1977). It shows intriguing behaviour with regular and periodic dips of intensity within its light curve (Walter et al., 1982; White and Swank, 1982). These dips usually occur on the time scale of the source’s orbital period (~ 50 min; Smale et al., 1988; Church et al., 1997) and are caused by the structure of the accretion disk obstructing our view of the central emission regions. Dipping systems are useful for researching the structure and properties of the accretion disk, as well as the geometry of the emission regions. The source also shows type-I X-ray bursts, indicating the central source to be a NS (Becker et al., 1977; Smale et al., 1988; Galloway et al., 2008).

The X-ray spectrum of XB 1916–053 can be well modelled with absorbed thermal emission from NS and accretion disk, and the thermal Comptonized emission (Bloser et al., 2000; Boirin et al., 2004; Zhang et al., 2014; Gambino et al., 2019). The spectrum of XB 1916–053 also shows absorption lines from highly ionized ions super-imposed on the continuum emission (Boirin et al., 2004; Iaria et al., 2006, 2021; Trueba et al., 2020). XB 1916–053 exhibits notable variations in its orbital period. The binary period is represented either by the X-ray dip period or the slightly ($\sim 1\%$) longer optical modulation period. Some studies have suggested that this discrepancy could be explained by the presence of a precessing accretion disk in the system, as described in the SU UMA model (White, 1989; Chou et al., 2001), or the possibility of a third body in a hierarchical triple system (Grindlay et al., 1988; Iaria et al., 2015). Additionally, Retter et al. (2002) reported a periodicity of 2979 seconds in the RXTE light curves, consistent with findings in earlier *Ginga* data (Smale et al., 1989). The 2979-second period was interpreted as a negative superhump or an infrahump, where the X-ray period is the orbital period of the system that beats with the nodal precession period of 4.86 days, suggesting the disk is tilted with respect to the equatorial plane (Retter et al., 2002; Hu et al., 2008).

In this work, we report the results of the spectral study of the persistent and dipping emission of XB 1916–053 by using the simultaneous *Chandra* and *Nuclear Spectroscopic Telescope Array (NuSTAR)* observation made during 2021. We report the detection of absorption features due to highly ionized materials during the persistent and dipping phases. We also report the update on the orbital ephemeris by including a newer dip arrival time measurement using the *NuSTAR* observation.

2. Observation and data reduction

The *NuSTAR* (Harrison et al., 2013) mission features two telescopes, focusing X-rays between 3 and 79 keV onto two identical focal planes (usually called focal plane modules A and B, or FPMA and FPMB). XB 1916–053 was observed with *NuSTAR* (obsID = 90701325002) on 2021-09-01 for an exposure of ~ 31 ks. We have used the most recent *NuSTAR* analysis software distributed with HEASOFT version 6.31.1 and the latest calibration files (version 20230124) for the reduction and analysis of the *NuSTAR* data. The calibrated and screened event files have been generated by using the task NUPIPELINE. A circular region of radius 80 arcsec centred at the source position was used to extract the source events. Background events were extracted from a circular region of the same size away from the source. The task NUPRODUCT was used to generate the light curves, spectra, and response files. The spectra were optimally binned using FTGROUPPHA by following the Kaastra and Bleeker (2016) optimal binning scheme with a minimum of 25 counts per bin. The FPMA and FPMB light curves were background corrected and summed using LCMATH. To perform the orbital phase-resolved spectroscopy and orbital timing study, photon arrival times were corrected to the Solar system barycentre using barycorr.

XB 1916–053 was observed simultaneously with *Chandra* using the ACIS/low energy transmission grating (LETG) for a total exposure of ~ 10 ks. To reduce pileup, the observation used a sub-array of 512 rows, yielding a frame time of 1.7 s. We ignored the zeroth-order events in our spectral analysis and used only the first-order grating spectra (e.g., Iaria et al., 2006, 2021). Data reduction was carried out using CIAO 4.17 with *Chandra* calibration database CALDB v.4.11.6. The standard processing was performed with the `chandra_repro` script to generate clean level 2 event files, source grating spectra, background spectra and response files. A background-corrected LETG light curve in the 1–8 keV energy range was extracted from a cleaned event file using `dmextract`. The `dmcopy` tool was used to apply the Good Time Interval (GTI) filtering to exclude the dipping events. The positive and negative first-order LETG spectra were combined using `combine-grating-spectra`, and the final spectrum was optimally rebinned following the Kaastra and Bleeker (2016) scheme.

We have used XSPEC (Arnaud, 1996) version 12.13.0c for the spectral fitting. The photo-electric absorption cross-section of Verner et al. (1996) and abundance of Wilms et al. (2000) have been used throughout. We have assumed the source distance to be equal to 9 kpc (Galloway et al., 2008). All the spectral uncertainties and the upper limits reported in this paper are at a 90% confidence level unless specified. All uncertainties from timing analysis are reported at a 68% confidence level unless specified.

3. Spectral analysis

Fig. 1 shows the background-corrected light curves of XB 1916–053 from *NuSTAR* and *Chandra* binned at 20 s in the energy range of 3–30 keV and 1–8 keV, respectively. The source light curve exhibited periodic absorption dips, as depicted in the top left panel of Fig. 1. The bottom panel shows the hardness ratio, which is a ratio of count rates in the energy range of 10–30 and 3–10 keV for *NuSTAR* and ratio in the 3–8 keV and 1–3 keV for *Chandra*. The hardness ratio values from *Chandra* have been shifted and adjusted for visualization purposes and do not represent absolute values. During the absorption dips, the hardness ratio notably increases due to the absorption of soft X-rays. The figure also includes the HID of XB 1916–053, shown in the right panel. In the HID, hardness represents the hardness ratio while intensity corresponds to the count rate in the 3–30 keV energy range.

Two methods were employed to extract spectra during the absorption dips and persistent emissions of XB 1916–053 from *NuSTAR*. In the first method, a count rate cut of 80% of the average persistent count rate of ~ 15 counts s^{-1} was applied. Segmentation was performed using 12 counts s^{-1} threshold (marked with a red dashed line in Fig. 1), resulting in segments representing the persistent and dip intervals (referred to as intensity-resolved spectra). GTIs were then created based on intensity filters, and spectra from FPMA and FPMB were extracted accordingly. In an alternative approach, spectra were extracted based on the orbital phase of XB 1916–053 (referred to as orbit-resolved spectra). Fig. 2 displays the orbital folded profile of the source at an orbital period of 3000.6511 seconds, with the dip center aligned at 0.5 phase. Dipping spectra were obtained from the 0.44–0.56 orbital phase (blue region in Fig. 2), while the persistent emission spectra were extracted from regions outside the dipping phase (black region in Fig. 2).

Similarly for *Chandra* data, the dipping intervals were excluded to extract the persistent spectrum, resulting in a net source exposure of 9 ks. Due to the limited exposure time of only ~ 500 s during the dipping phase, we did not use *Chandra* data for the dipping study.

3.1. Persistent spectra

3.1.1. NuSTAR

The spectra extracted from *NuSTAR*-FPMA and *NuSTAR*-FPMB observations were fitted simultaneously. We have added a constant to account for the cross-calibration of two instruments. The value of constant for

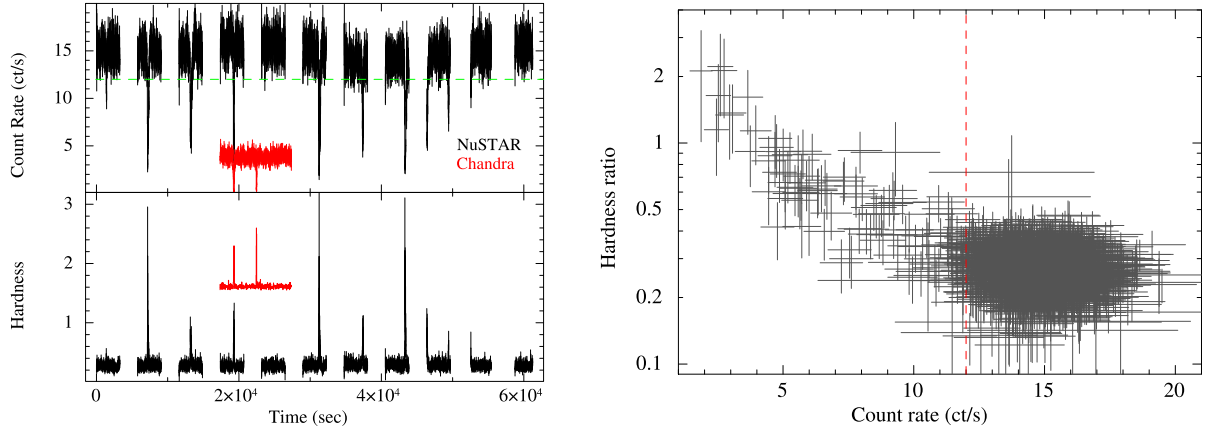


Fig. 1. *Left:* The light curve of XB 1916–053 from *NuSTAR* and *Chandra*/LETG binned at 20 s. The horizontal dashed green line marks the division of the persistent and dipping regions for *NuSTAR*. The bottom panel shows the hardness ratio, calculated as the ratio of count rates in the energy range of 10–30 and 3–10 keV for *NuSTAR* and in the 3–8 keV and 1–3 keV for *Chandra*. Note that the *Chandra* hardness ratio values have been shifted and adjusted for visualization purposes and do not represent absolute values. *Right:* Hardness-intensity diagram (HID) from *NuSTAR* data, where hardness is the ratio between count rates in 10–30 and 3–10 keV, and intensity is the count rate in the 3–30 keV energy range. The vertical dashed red line marks the division between the persistent and dipping regions.

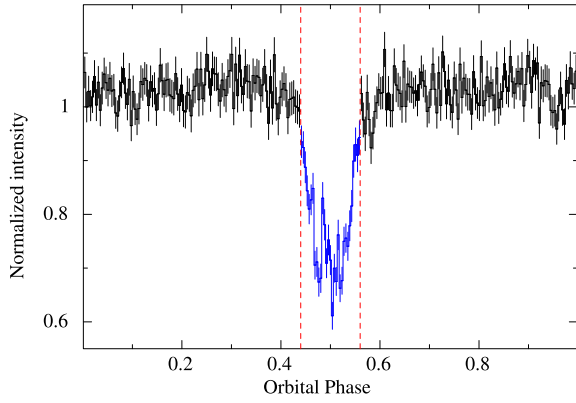


Fig. 2. The folded light curve of XB 1916–053 at an orbital period of 3000.6511 s. The 0.5 phase marks the dip arrival time at MJD 59458.14333. The dipping region is marked with a blue colour in the 0.44–0.56 phase (between red dashed vertical lines).

NuSTAR-FPMA was fixed to 1 and set free for FPMB. The *NuSTAR* data in the 3–75 keV energy range were used for spectral fitting.

The persistent spectrum of XB 1916–053 was modelled using the thermal Comptonization model thcomp (Zdziarski et al., 2020), which describes spectra from Comptonization by thermal electrons emitted by a spherical source with the sinusoidal-like spatial distribution of the seed photons. Compared to the widely used nthcomp model, thcomp agrees much better with actual Monte Carlo spectra from Comptonization (Zdziarski et al., 2020). Being a convolution model, thcomp allows for the Comptonization of various seed photon distributions (e.g., blackbody or disk blackbody), capturing both upscattering and downscattering effects (see, Zdziarski et al., 2020). The model also provides a correct description of Comptonized spectra at energies comparable to those of the seed photons and involves four parameters: asymptotic power-law photon index (Γ), electron temperature (kT_e), covering fraction (f_{cov}) and redshift which was fixed to zero in our analysis. Since the interstellar absorption is often poorly constrained in *NuSTAR* owing to a low energy threshold of 3 keV, N_H was fixed to $1.65 \times 10^{21} \text{ cm}^{-2}$ (see, section 3.1.3).

Regardless of the assumed seed photon sources, absorbed thermal Comptonization models with either blackbody or disk blackbody seeds failed to provide a satisfactory fit (Model M1 and M2; Table 1), primarily due to residuals in the 6–9 keV range, likely caused by multiple absorption features. To account for these, we incorporated a photo-ionized

Table 1
Best-fit statistics of different spectral models used.

S. No.	Model	χ^2/dof <i>NuSTAR</i>	C-stat/dof <i>Chandra</i> + <i>NuSTAR</i>
M1	$\text{tbabs}*\text{thcomp}*\text{BB}$	472/323	1305/743
M2	$\text{tbabs}*\text{nthcomp}*\text{diskBB}$	440/323	1231/743
M3	$\text{tbabs}*\text{zxcipcf}*(\text{thcomp}*\text{BB})$	419/320	1141/740
M4	$\text{tbabs}*\text{zxcipcf}*(\text{thcomp}*\text{diskBB})$	368/320	1103/740
M5	$\text{tbabs}*\text{zxcipcf}*(\text{thcomp}*\text{diskBB}+\text{BB})$	313/318	775/738
M6	$\text{tbabs}*\text{zxcipcf}*(\text{diskBB}+\text{thcomp}*\text{BB})$	301/318	762/738

absorber, zxcipcf (Reeves et al., 2008), a model commonly used to describe absorption features in NS LMXBs (e.g., Ponti et al., 2015; Raman et al., 2018; Sharma et al., 2018; Gambino et al., 2019). While the addition of zxcipcf (Models M3 and M4) improved the fit, it remained statistically unsatisfactory (Table 1).

Further improvement was achieved by including an additional soft thermal component, leading to a three-component model comprising two soft thermal components (from the accretion disk and NS surface) and a Comptonized component originating from either of thermal seed (Lin et al., 2007; Sharma et al., 2018; Gambino et al., 2019). This addition of an additional soft component further improved the fit to $\chi^2/\text{dof} = 313/318$ and $\chi^2/\text{dof} = 301/318$ for models M5 (disk blackbody seeds) and M6 (blackbody seeds), respectively, with a probability of chance improvement (PCI) of $< 10^{-11}$. Notably, the Comptonization associated with the NS blackbody (Model M6) was favourable over Model M5 as it resulted in better-fit statistics and PCI of 5×10^{-4} . To further assess the significance of this result, we simulated 1000 spectra and fitted them with models M5 and M6 to derive a distribution of fit statistics for both models. A Kolmogorov-Smirnov (KS) test¹ was performed to compare the two samples, confirming that Model M6 describes the spectra more accurately, with a p-value of 0.0026. The χ^2/dof values obtained from the different models used are summarized in Table 1. A more complex double-seed Comptonization model ($\text{tbabs}*\text{zxcipcf}*(\text{thcomp}*\text{diskbb} + \text{thcomp}*\text{BB})$) was statistically insignificant (Zhang et al., 2014; Gambino et al., 2019), and f_{cov} for disk seed Comptonization was found to be only 7×10^{-4} , further supporting the dominance of blackbody as the primary seed photon source.

¹ https://docs.scipy.org/doc/scipy/reference/generated/scipy.stats.ks_2samp.html.

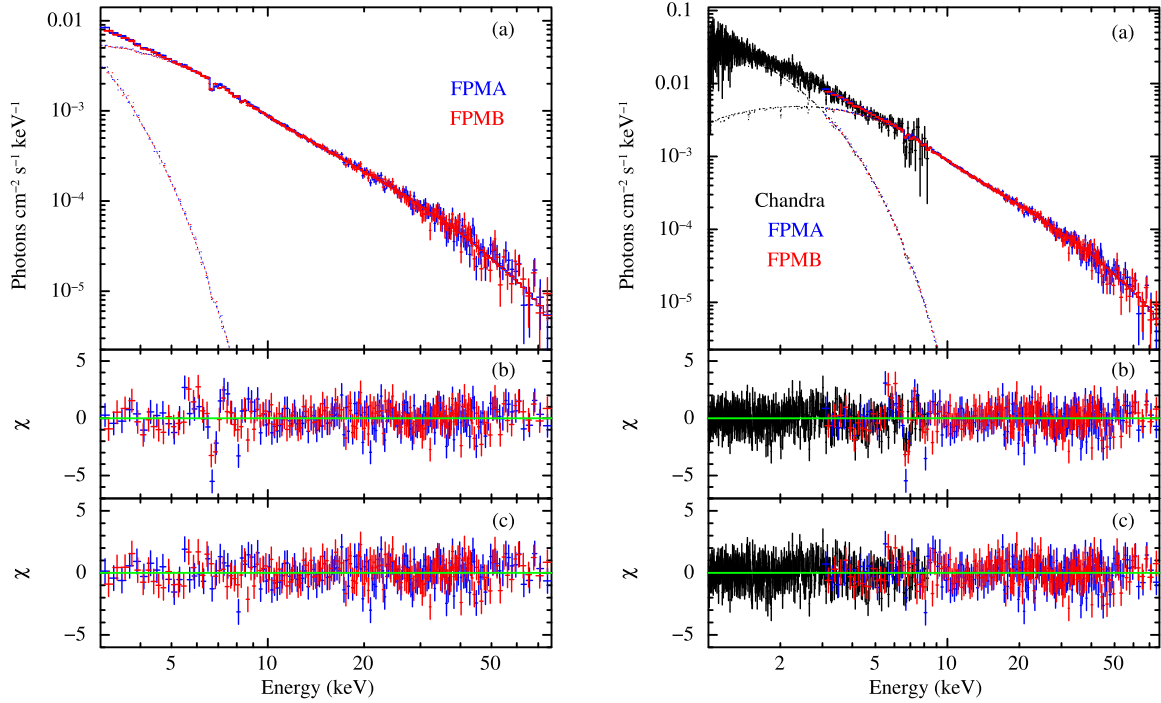


Fig. 3. *Left:* (a) The Persistent spectrum of XB 1916–053 from the *NuSTAR* observation fitted with a model comprising a multi-coloured disk blackbody (`diskbb`) and single-temperature blackbody (`bbodyrad`) that is Comptonized (`thcomp`), with absorption from neutral (`tbabs`) and ionized (`zxcipcf`) material. (b) Residuals ($\chi = (\text{data} - \text{model}) / \text{error}$) after fitting only the continuum model (excluding ionized absorption), showing prominent absorption features in the 6–10 keV range, primarily due to Fe K absorption at 6.7 keV and 8 keV. (c) Residuals from the best-fit model `tbabs*zxcipcf*(diskbb+thcomp*BB)` show a satisfactory fit, with `zxcipcf` component accounting for the narrow Fe K absorption lines. *Right:* Same as the left panel, but for the persistent spectrum using a joint fit of *Chandra*+*NuSTAR*.

A similar trend was observed in the orbit-resolved persistent spectrum, suggesting the presence of two soft thermal components and Comptonized emission with blackbody as the dominant source of seed photons. Hence, all results reported in this paper are based on intensity-resolved spectra.

Since the covering fraction of `zxcipcf` was pegged at 1, we fixed it under the assumption that the ionized absorber fully covered the central emission region. Allowing the redshift parameter (z) of `zxcipcf` to vary did not improve the fit, yielding a best-fit value consistent with zero, indicating a static accretion disk atmosphere. Consequently, z of `zxcipcf` was fixed to zero. Using high-resolution *Chandra* spectra, Trueba et al. (2020) also suggested the bulk of absorption from static disk atmosphere located close to the compact object with a redshift of $\sim 220 - 290 \text{ km s}^{-1}$. The best-fit parameters obtained from Model M6 are presented in Table 2. The corresponding best-fit spectrum is shown in the left panel of Fig. 3(a) with residuals from the best-fit model in Fig. 3(c). For comparison, Fig. 3(b) shows best-fit residuals without `zxcipcf` and only continuum emission, highlighting the presence of an ionized absorber.

Two major absorption features were observed in the spectrum at $6.75^{+0.18}_{-0.05} \text{ keV}$ and $8.09^{+0.08}_{-0.45} \text{ keV}$ with equivalent widths of $-42^{+15}_{-21} \text{ eV}$ and $-24^{+13}_{-22} \text{ eV}$, respectively. The significance of lines are around ~ 9 and $\sim 4.3\sigma$, respectively, based on the ratio of the line normalization to its one-sigma error. The absorption line observed at $\sim 6.75 \text{ keV}$ may be interpreted as a $K\alpha$ line from He-like and H-like iron. The absorption feature at $\sim 8 \text{ keV}$ may be produced by a blend of the $K\beta$ absorption lines from He-like/H-like iron (at 7.88 keV/8.26 keV) and He-like/H-like nickel (at 7.77–7.81 keV/8.07–8.10 keV). Similar absorption-line features at these energies have been previously observed in XB 1916–053 (Boirin et al., 2004; Iaria et al., 2006; Zhang et al., 2014; Gambino et al., 2019) and in other NS LMXBs (Sidoli et al., 2002; Díaz Trigo et al., 2006; Hyodo et al., 2009; Ponti et al., 2015; Sharma et al., 2018).

3.1.2. *Chandra*

The grating spectrum was fit in the 1–8 keV range due to poor signal-to-noise outside this energy range. C-stat was used as fitting statistics (Cash, 1979). The continuum can be well-fitted with absorbed power-law with an equivalent hydrogen column density of $N_H = 4.3(2) \times 10^{21} \text{ cm}^{-2}$, a photon index of 1.84 (2), and a power-law normalization of 0.071 (8), consistent with Iaria et al. (2006). The presence of several absorption features was clearly evident in the residuals. Due to the low signal-to-noise ratio, we could not extract detailed information about the absorption lines and instead focused on their detection. To do so, we modelled each feature using a Gaussian line with negative normalization. We identified seven absorption lines centred at 2.008 (5), 2.639 (7), 3.106 (12), 3.273 (18), $4.128^{+0.029}_{-0.009}$, 6.66 (5) and $6.99^{+0.08}_{-0.06} \text{ keV}$, corresponding to Si XIV, S XVI, S XVI $K\beta$ /Ar XVII, Ar XVIII, Ca XX, Fe XXV and Fe XXVI, respectively. Their equivalent widths were 3.9 ± 2.9 , 8 ± 4 , 8 ± 5 , 11 ± 5 , 13 ± 9 , 110 ± 40 , and $98 \pm 59 \text{ eV}$, respectively. Additionally, we detected an absorption feature at $1.522^{+0.004}_{-0.006} \text{ keV}$, with an equivalent width of $2.9 \pm 1.7 \text{ eV}$. This feature could be associated with the Fe-complex or an instrumental feature. In Fig. 4, we present the flux spectrum in the narrow energy range of 1.4–5 keV, highlighting the detected absorption features.

3.1.3. *Chandra*+*NuSTAR*

As the *Chandra* data is contemporaneous to *NuSTAR*, we performed a joint fit, extending the low energy coverage down to 1 keV. Similar to the *NuSTAR*-only spectra, the joint spectra continuum is well-described by the two soft thermal components and a thermal Comptonized component (Table 1). However, a degeneracy was observed between Models M5 and M6, as these two models can not be distinguished based on fit statistics. We also assessed this further by simulation of 1000 spectra but found that the distributions of fit statistics of both models were nearly identical. We also tested a double-seed Comptonization model (`tbabs*zxcipcf*(thcomp*diskbb + thcomp*BB)`), but it was statistically insignificant. However, this model suggested a blackbody cov-

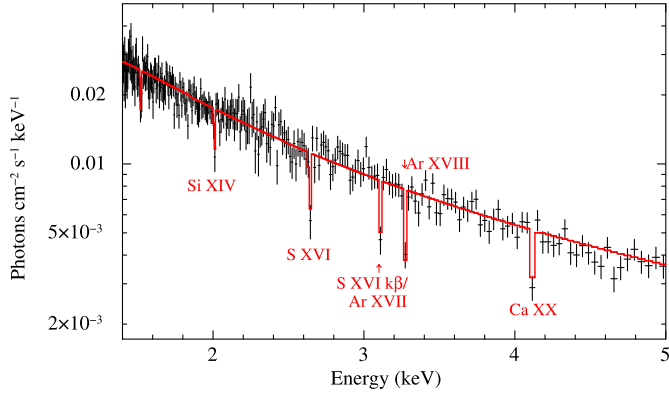


Fig. 4. Flux spectra and best-fit model for the combined first-order LETG *Chandra* spectrum of XB 1916–053. For visual clarity, only the 1.4–5 keV range is shown. The solid red line represents the best-fit model, incorporating both the continuum and absorption features from silicon, sulfur, argon, and calcium, which are labelled in the figure.

Table 2

Best-fit spectral parameters of XB 1916–053 during the persistent emission. All errors and upper limits reported in this table are at a 90% confidence level ($\Delta\chi^2 = 2.7$).

Component	Parameters	<i>NuSTAR</i>		
		M6	<i>Chandra+NuSTAR</i>	
			M6	M5
tbabs	N_H (10^{21} cm $^{-2}$)	1.65 ^{fixed}	1.65 ± 0.80	1.8 ^{+1.0}
zxcpcf	N_H (10^{22} cm $^{-2}$)	11.5 ^{+15.0} _{-6.3}	35 ⁺²² ₋₁₂	42 ⁺³⁸ ₋₁₅
	log ξ	3.8 ± 0.3	4.17 ^{+0.11} _{-0.13}	4.19 ^{+0.10} _{-0.12}
diskbb	kT_{in} (keV)	0.57 ^{+0.09} _{-0.08}	0.73 ± 0.05	0.61 ^{+0.07} _{-0.09}
	Norm	118 ⁺²¹¹ ₋₇₀	28.7 ^{+9.3} _{-7.0}	61 ⁺⁴⁹ ₋₂₁
BBbodyrad	$^b R_{in}$ (km)	23 ⁺²⁰ ₋₇	11.2 ^{+1.8} _{-1.4}	16.4 ^{+6.6} _{-2.8}
	kT_{BB} (keV)	1.25 ^{+0.08} _{-0.07}	1.37 ± 0.08	1.66 ± 0.08
thcomp	Norm	8.5 ^{+2.0} _{-1.9}	5.8 ^{+1.4} _{-1.1}	0.62 ^{+0.18} _{-0.16}
	R_{BB} (km)	2.6 ± 0.3	2.17 ^{+0.20} _{-0.26}	0.71 ^{+0.10} _{-0.09}
Cons	Γ	1.93 ± 0.05	1.93 ± 0.06	1.85 ± 0.04
	kT_e (keV)	16.4 ^{+3.9} _{-2.4}	17.5 ^{+5.1} _{-2.8}	14.6 ^{+2.3} _{-1.6}
Flux ^a	f_{cov}	0.75 ^{+0.07} _{-0.03}	0.76 ^{+0.08} _{-0.06}	0.69 ^{+0.12} _{-0.09}
	τ	3.9 ± 0.7	3.75 ± 0.7	4.5 ± 0.6
Flux ^a	C_{FPMB}	0.986 ± 0.006	0.986 ± 0.006	0.986 ± 0.006
	$C_{Chandra}$		0.99 ± 0.02	0.99 ± 0.02
	F_{3-78}^{Total} keV	4.2×10^{-10}	4.3×10^{-10}	4.3×10^{-10}
	$F_{0.1-100}^{Total}$ keV	7.1×10^{-10}	6.2×10^{-10}	6.2×10^{-10}
	$F_{0.1-100}^{diskbb}$ keV	2.5×10^{-10}	1.7×10^{-10}	1.8×10^{-10}
	$F_{0.1-100}^{BB}$ keV	2.2×10^{-10}	2.2×10^{-10}	0.5×10^{-10}
	$F_{0.1-100}^{comp}$ keV	2.3×10^{-10}	2.2×10^{-10}	3.9×10^{-10}
	χ^2/dof	301.5/319		
	C-stat/dof		762/738	774.6/738

^a Unabsorbed flux in units of erg cm $^{-2}$ s $^{-1}$.

^b For assumed inclination angle of 75°.

ering fraction (f_{cov}) of 0.75^{+0.07}_{-0.12}, while for the *diskbb*, f_{cov} was only 6×10^{-4} with an upper limit of 0.38. This implies that the corona predominantly covers the blackbody source, making it the primary seed photon source. Despite these results, Model M5 cannot be statistically ruled out. The best-fit parameters for Models M5 and M6 are presented in Table 2. The best-fit spectrum with M6 is shown in the right panel of Fig. 3. The spectral parameters remain consistent with those obtained from the *NuSTAR*-only spectra. However, a discrepancy is observed with *diskbb* component, likely due to the limited low-energy coverage of *NuSTAR*, which affects the disk component constraints. Differences in the ionized absorber were also observed between the two spectra, possibly due to the presence of highly ionized absorption lines in the *Chandra* spectra, consistent with Gambino et al. (2019); Iaria et al. (2021). The inclusion of an additional absorber did not provide any improvement to the fit.

Table 3

Best-fit spectral parameters of XB 1916–053 during the dipping emission, with the continuum fixed to the persistent emission. All errors and upper limits reported in this table are at a 90% confidence level ($\Delta\chi^2 = 2.7$).

Component	Parameters	1-Absorber	2-Absorber
zxcpcf	N_H (10^{22} cm $^{-2}$)	79 ⁺⁸ ₋₇	73 ⁺⁸ ₋₇
	log ξ	2.09 ^{+0.13} _{-0.14}	2.03 ^{+0.12} _{-0.21}
	Cov. frac.	0.65 ± 0.03	0.63 ± 0.03
	C_{FPMB}	0.967 ± 0.03	0.965 ± 0.030
	χ^2/dof	167.5/136	168/136

The unabsorbed flux of both the total emission and individual spectral components was calculated using *cflux* convolution model in XSPEC. The total unabsorbed flux in the 0.1–100 keV energy range was estimated to be $\sim 6.2 \times 10^{-10}$ erg cm $^{-2}$ s $^{-1}$, corresponding to an X-ray luminosity of $\sim 6 \times 10^{36}$ erg s $^{-1}$. For Model M6, the emission from the accretion disk contributes around 28% of the total emission, while the emission from the NS contributes around 72%, with equal parts being directly observed and Comptonized. Similar flux distribution was also observed with *Suzaku* spectra from 2006 (Gambino et al., 2019). In contrast, Model M5 exhibits a drastically different flux contribution, where the NS accounts for only 8% of the total flux, while the accretion disk dominates with 92%, of which 32% is directly observed, and 60% is Comptonized. Notably, the flux estimated from *NuSTAR*-only spectra is higher due to poorly constrained disk blackbody component, emphasizing the need for broadband spectral coverage to accurately model soft emission components, such as accretion disks in LMXBs.

3.1.4. Dipping spectra

To investigate the effect of absorption dips, a spectrum from the dipping region was extracted using both methods described earlier in Section 3. Assuming the dipping activity arises from absorption caused by the passage of the vertical structures obscuring our view to the source (Díaz Trigo et al., 2006) and the underlying continuum spectrum remains constant throughout the observation, any spectral variations observed during the dipping intervals are attributed solely due to the passage of this absorbing material along our line of sight. Therefore, a continuum similar to the best-fit persistent spectrum was used to describe the dip spectrum, with fixed continuum model parameters except for the ionized absorption component. Initially, we assumed a single absorber for the dipping phase. The dipping absorber was found to have a column density of $\sim 8 \times 10^{23}$ cm $^{-2}$, a low ionization parameter of log $\xi \sim 2$ and a covering fraction of 65%.

As the persistent emission also shows the presence of an ionized absorbing medium from the accretion disk atmosphere, hence two absorbers may be present during dipping activity, one from the accretion disk atmosphere and the other from the vertical structure near the bulge where the accretion stream encounters the rim of the disk (e.g., Trueba et al., 2020). Therefore, we also used two ionized absorber components in which the first absorber was fixed to match the persistent emission, accounting for the accretion disk atmosphere. Fitting the dip spectrum with either a 1-absorber or 2-absorber model resulted in comparable fit statistics, with parameter values consistent within uncertainties (see Table 3). Fig. 5(a) shows the comparison of the persistent and dipping spectra, while panel (b) shows residuals of the dipping spectrum compared to the best-fit model of the persistent spectrum, highlighting significant absorption of soft X-ray emission primarily below 15 keV. Fig. 5(c) shows the residuals with the best-fit dipping spectra with the 2-absorber model.

The orbit-resolved dip spectrum resulted in similar absorbing column density and ionization parameter. However, a lower value of the covering fraction ($\sim 40\%$) was observed for both 1-absorber and 2-absorber models, possibly due to orbit-to-orbit variation of dipping intervals (Raman et al., 2018).

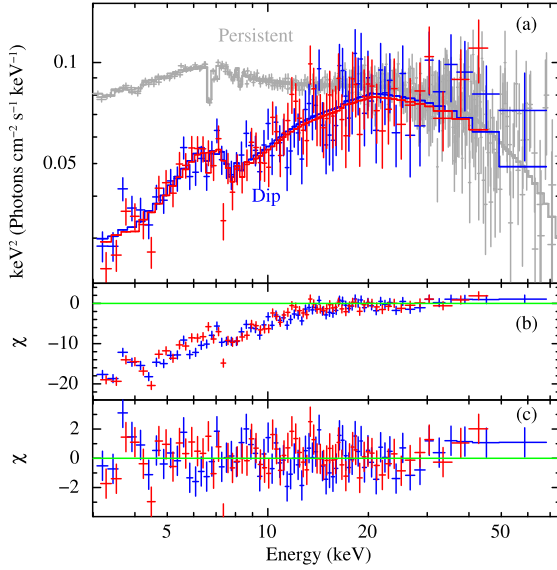


Fig. 5. (a) A comparison between persistent and dip spectrum of XB 1916–053. The persistent spectrum is shown in grey, while dip spectra are in blue (FPMA) and red (FPMB). The dip spectrum is fitted with the same model as persistent spectra with continuum parameters fixed. An additional ionized absorber component was added to account for dips (2-Absorber model). b) Residuals showing the contribution of the ionized absorber during dipping compared to the persistent emission. c) Residuals from the best-fit model for the dipping intervals.

3.2. Update on orbital ephemeris

We folded the *NuSTAR* light curve adopting a reference period of 3000.6511 s (Iaria et al., 2015). To estimate the dip arrival time, the folded profile was modelled with a step-ramp function. A dip arrival time of MJD 59458.14333 (6) was obtained. Adopting a reference orbital period of $P_{\text{orb}} = 3000.6511$ sec and reference epoch $T_0 = 50123.00873$ MJD, the orbital cycle number $N = 268793$ was inferred. The delay associated was found to be 1618 (5) sec with reference to constant orbital period. We included this measured dip arrival time and delay with those reported in Iaria et al. (2015, 2021) to update the orbital ephemeris.

Following Iaria et al. (2015, 2021), we fitted the delays as a function of dip arrival time adopting the linear+quadratic (LQ) model $y = a + bt + ct^2$, where $a = \Delta T_0$ is a correction to the reference epoch T_0 , $b = \Delta P_{\text{orb}}/P_{\text{orb}}$ in units of s d^{-1} with ΔP_{orb} is correction to the adopted orbital period and $c = 0.5P_{\text{orb}}/\dot{P}_{\text{orb}}$ in units of s d^{-2} which give the measure of orbital period derivative \dot{P}_{orb} . As reported by Iaria et al. (2015, 2021), the LQ model is not a good estimate of the measured delays of XB 1916–053 and yielded a χ^2/dof of 363/28. The residuals showed systematic variations mimicking sinusoidal variations.

To address this, we added a sinusoidal term to the LQ model, resulting in the LQS model such that $y = a + bt + ct^2 + A \sin(2\pi(t - \phi)/P_{\text{mod}})$, where A is the amplitude of the sinusoidal function in seconds, P_{mod} is the period of the sine function in days, and ϕ is the time at which the sinusoidal function is null. The LQS model improves the fit significantly to χ^2/dof of 45/25 with an F -test probability of 1.8×10^{-11} . Notably, the best-fit residuals exhibited no further systematic variations. The resultant best-fit values are reported in Table 4 along with a comparison to the previously reported results by Iaria et al. (2021). Fig. 6 illustrates the fit to the delays and the corresponding best-fit residuals, which manifest sinusoidal variations indicative of the underlying orbital dynamics. The obtained orbital ephemeris is largely consistent with that reported by Iaria et al. (2021) and given as:

Table 4

Best-fit values of the functions adopted to fit the delays. All errors reported in this table are at 68% confidence level ($\Delta\chi^2 = 1$).

Parameters	Iaria et al. (2021)	This work
a (s)	14 ± 14	0.9 ± 14
b (10^{-3} s d^{-1})	5 ± 3	7 ± 2
c (10^{-5} s d^{-2})	1.82 ± 0.04	1.85 ± 0.04
T_0 (MJD)	50123.0089 ± 0.0002	50123.00874 ± 0.00016
P_{orb} (s)	3000.65129 ± 0.00008	3000.65136 ± 0.00008
\dot{P}_{orb} (s s^{-1})	$(1.46 \pm 0.03) \times 10^{-11}$	$(1.49 \pm 0.03) \times 10^{-11}$
A (s)	130 ± 14	146 ± 13
ϕ (d)	1262 ± 133	1230 ± 122
P_{mod} (d)	9099 ± 302	8845 ± 243
χ^2/dof	37/24	45/25

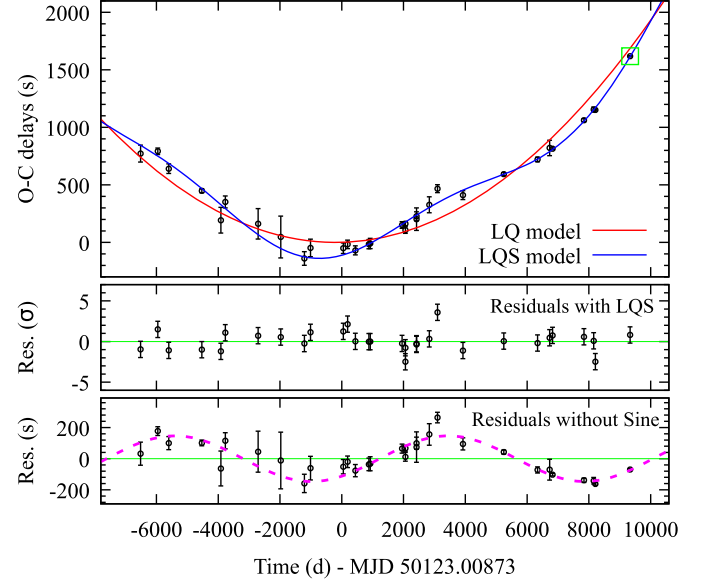


Fig. 6. *Top panel:* Delays vs time. The red curve represents the best fit for the LQ function, while the blue curve represents the best fit for the LQS function. The *NuSTAR* observation is highlighted by the green box. *Middle panel:* Residuals in units of sigma ($\sigma = (\text{data-model})/\text{error}$), corresponding to the LQS model. *Bottom panel:* Residuals in units of seconds, without the sine function. The magenta line shows the sinusoidal variations due to the presence of a third body.

$$T_{\text{dip}}(N) = 50123.00874(16) \text{ MJD} + \frac{3000.65136(8)}{86400} N + 2.59(6) \times 10^{-13} N^2 + \frac{A}{86400} \sin\left(\frac{2\pi}{P_{\text{mod}}}(t - \phi)\right) \quad (1)$$

with $P_{\text{mod}} = 8845 \pm 243$ d (24.2 ± 0.7 yr), $\phi = 1230 \pm 122$ d, and $A = 146 \pm 13$ s. The corresponding orbital period derivative is $\dot{P}_{\text{orb}} = 1.49(3) \times 10^{-11} \text{ ss}^{-1}$. Further, the addition of a cubic term to the LQ or LQS model does not improve the fit to delays.

4. Discussion and conclusions

In this study, we performed a comprehensive spectral and timing analysis of the NS LMXB XB 1916–053 using contemporaneous *Chandra* and *NuSTAR* observations from 2021. Our analysis presents the emission properties of the system during persistent and dipping intervals, highlighting the complexity of the X-ray spectrum and the significant role of ionized absorbers.

4.1. Persistent emission

The broad-band X-ray spectra of XB 1916–053 in the persistent state can be effectively modelled with a combination of a blackbody, disk blackbody, and thermal Comptonized emission. Our study supports the

NS surface (or boundary layer) as the dominant source for the Comptonization seed photons yielding the observed hard emission (Model M6). However, a contribution from the accretion disk (Model M5) cannot be ruled out based on fit statistics, suggesting a possible mix of both seed sources. The broadband coverage reveals that the accretion disk has a much lower covering fraction compared to the NS surface, reinforcing the blackbody seed as the most suitable model.

Based on our modelling, the accretion disk extends close to the NS surface or forms a boundary layer, with matter accreting primarily along an equatorial zone and emitting blackbody radiation. This emission is then moderately Comptonized by the hot corona. The electron temperature of Comptonizing plasma was found to be ~ 17 keV with an optical depth of ~ 4 . This temperature is notably higher than the previous report for XB 1916–053 in the soft state (Zhang et al., 2014; Gambino et al., 2019), indicating a harder spectrum compared to the earlier *Suzaku* observations. The estimated broadband flux in our analysis is comparable to that observed with *Suzaku* (Zhang et al., 2014; Gambino et al., 2019). Although the exact geometry of the corona remains uncertain, our spectral modelling and parameter estimates suggest an optically thick, compact corona surrounding the NS (similar to the single seed geometry given in Fig. 3(a) of Zhang et al., 2014). Dipping LMXBs in the soft state are known to exhibit systematically harder spectra compared to non-dipping LMXBs (Gladstone et al., 2007). This spectral hardening can be attributed to the oblate shape of the Comptonizing corona, where up-scattered photons travel a longer path along the line of sight (Zhang et al., 2014, 2016; Sharma et al., 2018). The observed electron temperature and optical depth are consistent with the hard state. However, the disk and blackbody temperatures, as well as their contributions to the total flux, suggest characteristics of the soft state (e.g., Armas Padilla et al., 2017; Sharma et al., 2018).

We have observed highly-ionized absorption lines from Si, S, Ar, Ca, Fe and a blend of highly ionized Fe $K\beta$ and Ni $K\alpha$ in the persistent X-ray spectrum, indicating the existence of a complex ionized absorber along the line of sight, with origins likely in the disk atmosphere (Díaz Trigo and Boirin, 2013). The ionized disk absorber has an absorption column density $\sim 10^{23}$ cm $^{-2}$ and an ionization parameter, $\log \xi \sim 4$. Previously, $K\alpha$ transition lines, as well as $K\beta$ transition lines of Fe were observed with *XMM-Newton*, *Chandra* and *Suzaku* (Boirin et al., 2004; Iaria et al., 2006; Juett and Chakrabarty, 2006; Gambino et al., 2019). Similar ionized absorbers have been observed in other high-inclination NS LMXBs, such as EXO 0748–676, AX J1745.6–2901, and MXB 1658–298, but only in their soft states (Ponti et al., 2014, 2015, 2019; Sharma et al., 2018). These features tend to disappear in the hard state due to thermal photoionization instability (Bianchi et al., 2017; Ponti et al., 2019). However, in the AMXP Swift J1749.4–2807, disk winds were observed in the intermediate or hard-intermediate state, proposed to be propeller-driven (Marino et al., 2022).

In order to corroborate the spectral state identification, we extracted the Leahy-normalised Fourier Power Density Spectrum (PDS) from the 3–30 keV persistent and average light curves, binned at 1 s. The PDS from the persistent light curve is consistent with a constant power of ~ 2 , compatible with Poisson noise. The fractional rms was measured to be ~ 3 –6%, suggesting very little X-ray variability. This contrasts with the behaviour of NS LMXBs in the hard state, which typically exhibits rms amplitudes of 10–20% or higher (see, e.g., Muñoz-Darias et al., 2014). Hence, the timing properties of XB 1916–053 during persistent emission more closely resemble those of a soft state, challenging the hard state identification. The PDS from the average light curve is dominated by red noise below 0.01 Hz with an rms of $\sim 14\%$ and is consistent with Poisson noise at higher frequencies. The enhanced variability at low frequencies in the average light curve can be attributed to dipping activity.

4.1.1. Inclination & magnetic field estimates

The emission from the accretion disk contributes around 28% to the total emission, while the NS accounts for the remaining 72%, with its emission split equally between direct observation and Comptonization.

In a standard accretion disk, half of the gravitational energy is expected to be radiated by the matter before it reaches the inner radius (R_{in}). The remaining half of the energy, along with the energy released from R_{in} to the NS radius, contributes to powering the blackbody emission from the NS surface/boundary layer and the corona. As a result, the disk luminosity is anticipated to be comparable to that of the Comptonized blackbody, however, the observed fluxes will vary depending on our viewing angle. Assuming the equatorial geometry of the blackbody-radiating area and corona around the NS, we can estimate the inclination angle i of the disk as

$$\tan i = \frac{\pi}{2} \frac{F_{\text{BB}}}{F_{\text{disk}}} \quad (2)$$

(Mitsuda et al., 1984; Sakurai et al., 2012). The observed ratio of F_{BB} to F_{disk} is 2.6, which helps to constrain the inclination angle to be around 76° , consistent with the expected range for dipping but not eclipsing source ($60^\circ \leq i \leq 75^\circ$; Frank et al., 1987).

The inner disk radius R_{in} can be estimated from `diskbb` normalization ($Norm_{\text{disk}}$) using $R_{\text{in}} = \alpha \kappa^2 (Norm_{\text{disk}} / \cos i)^{1/2} D_{10}$ km, where D_{10} is the distance to the source in units of 10 kpc, i is the inclination angle of disk, and $\alpha = 0.41$ and $\kappa = 1.7$ are correction factors (Mitsuda et al., 1984; Shimura and Takahara, 1995; Kubota et al., 1998). The inner disk radius of $11.2^{+1.8}_{-1.4}$ km is estimated assuming the inclination angle of 75° (Frank et al., 1987). However, the value of the inner disk radius is uncertain, subject to the uncertainty in the disk inclination angle i . Similarly, the size of the blackbody emitting region can be estimated using the normalization of `bodyrad` model, which scales as $(R_{\text{BB}}/D_{10})^2$. The normalization of the blackbody component implies an emitting region size of $R_{\text{BB}} \sim 2$ km, indicating that the blackbody emission arises from an equatorial belt-like region on the NS surface (Lin et al., 2007). In contrast, Gambino et al. (2019) reported a larger seed photon radius of ~ 10 –14 km and an inner disk radius of ~ 30 km, albeit with larger uncertainty. Our analysis provides a more precise estimate of both the inner disk radius and seed photon radius, which are consistent with the soft spectral state. This improvement is likely due to a more appropriate model selection for describing the continuum, the broadband spectral coverage provided by *Chandra* and *NuSTAR*, and their superior spectral resolution. The relatively small blackbody radius can be explained if a geometrically thin accretion stream deposits matter onto a well-defined impact region near the NS equator, where the accreting material efficiently releases energy before gradually spreading across the stellar surface (Lin et al., 2007).

The inferred inner disk radius of ~ 11 km suggests that the accretion disk extends moderately close to the NS surface, leading to the formation of a boundary layer around the NS (Popham and Sunyaev, 2001). To investigate the extent of the boundary layer, we use the mass accretion rate (\dot{M}) to estimate its maximum radial extent. According to Equation 25 of Popham and Sunyaev (2001), the maximum radial extent of this region can be estimated as

$$\log(R_{\text{max}} - R_{\star}) \simeq 5.02 + 0.245 \left| \log \left(\frac{\dot{M}}{10^{-9.85} M_{\odot} \text{yr}^{-1}} \right) \right|^{2.19} \quad (3)$$

We determine the mass accretion rate using the unabsorbed luminosity from 0.1–100.0 keV and an accretion efficiency of $\eta = 0.2$ to be $5.13 \times 10^{-10} M_{\odot} \text{yr}^{-1}$. This gives a maximum radial extent of $5.44 R_g$ for the boundary layer, which is 1.2 km from the NS surface. This value is consistent with the estimated location of the inner disk radius.

We can also estimate limits on the magnetic field strength assuming the inner accretion disk is truncated at magnetospheric radius (Cackett et al., 2009; Degenaar et al., 2014; Sharma et al., 2019). To calculate the magnetic field strength (B), we have used the following expression originally given by Ibragimov and Poutanen (2009),

$$B = 1.44 \times 10^7 k_A^{-7/2} \left(\frac{M_{\text{NS}}}{1.4 M_{\odot}} \right)^{1/4} \left(\frac{R_{\text{in}}}{10 \text{ km}} \right)^{7/4} \left(\frac{R_{\text{NS}}}{10^6 \text{ cm}} \right)^{-3} \times \left(\frac{f_{\text{ang}}}{\eta} \frac{F_{\text{bol}}}{10^{-9} \text{ erg cm}^{-2} \text{ s}^{-1}} \right)^{1/2} \left(\frac{D}{9 \text{ kpc}} \right) \text{ G}, \quad (4)$$

where k_A represents the geometry coefficient with a permissible value of 0.5–1.1 (Psaltis and Chakrabarty, 1999; Long et al., 2005; Kluźniak and Rappaport, 2007), f_{ang} is the anisotropy correction factor which is approximately unity (Ibragimov and Poutanen, 2009), and η is the accretion efficiency factor. We have assumed $k_A = 0.5$, $\eta = 0.2$, $f_{\text{ang}} = 1$, $D = 9$ kpc, and a reasonable NS mass and radius of $M_{\text{NS}} = 1.4M_{\odot}$ and $R_{\text{NS}} = 10$ km, respectively, along with the average 0.1–100 keV bolometric flux of 6.2×10^{-10} erg cm⁻² s⁻¹ from our best-fitting results. We estimate the upper limit of the magnetic field strength to be $B < 4.5 \times 10^8$ G, considering an upper limit of 13 km on the inner disk radius. This estimate is consistent with the magnetic field strengths of several NS LMXBs and accreting millisecond X-ray pulsars (Mukherjee et al., 2015; Ludlam et al., 2017; Sharma et al., 2019, 2020b; Beri et al., 2023). If the accretion disk is indeed truncated by the NS's magnetic pressure, with matter funnelled along magnetic field lines, one would typically expect X-ray pulsations provided that the spin and magnetic axes are misaligned. However, no pulsations have been detected from XB 1916–053. While the system's high inclination could play a role, this alone cannot fully explain the absence of pulsations, as X-ray pulsations have been observed in highly inclined sources such as XB 1822–371 (e.g., Anitra et al., 2021; Iaria et al., 2024). Therefore, a weak magnetic field strength that is insufficient to channel the accreting matter to magnetic poles remains a plausible explanation for the lack of detected pulsations.

4.2. Dipping emission

The continuum model used for persistent spectra also provides a good fit for the spectrum during dipping. For the dip spectrum, the parameters of the continuum were fixed to the persistent values, while the parameters of the ionized absorbers (`zxipcf`) were allowed to vary. The dip spectra show significant changes attributed to the increased absorption column density ($\sim 8 \times 10^{23}$ cm⁻²) and a lower ionization parameter ($\log \xi \sim 2$). These variations are likely due to the obscuration by denser, less ionized material near the outer disk or bulge. In XB 1916–053 and other dippers, particularly strong absorption lines are detected during dipping events and are typically associated with the outermost edge of the accretion disk (Díaz Trigo et al., 2006).

Since dip spectra are affected by absorption from both the inner disk atmosphere and the outermost disk, therefore, we added an additional absorber component with the first absorber component fixed to the parameters of the accretion disk absorber from the persistent emission. However, no significant difference was found between the 1-absorber and 2-absorber models. During dipping, the ionized plasma exhibited a lower ionization parameter and a higher column density. The transition from the persistent to the dip spectrum can thus be explained as a decrease of the ionization parameter ξ of the plasma with a simultaneous increase of the equivalent hydrogen column density of an ionized absorber interposed between the observer and the central emitting source (Boirin et al., 2004). The lack of a significant difference between the 1-absorber and 2-absorber models suggests that the absorption is likely coming from a continuous structure whose properties evolve between the persistent and dipping states rather than from two well-separated regions. It could be possible that the absorbing medium is relatively homogeneous in structure, gradually increasing in density and decreasing in ionization as the system moves into the dipping phase, as the line of sight intercepts a denser but not strongly fragmented region.

During persistent intervals, the ionized plasma transmits all photons except those with energies matching different ions' transitions, such as highly ionized Fe K_{α} and K_{β} and Ni ions transitions. This results in significant absorption of photons during persistent intervals. Similarly, atomic transitions and edges from many ions affect the transmission during the dipping intervals as the ionization is lower, leading to a strongly energy-dependent transmission. During dipping, edges are stronger because of the larger column density.

4.3. Orbital

Previously, Iaria et al. (2021) studied the orbital evolution of XB 1916–053 with 40 years of baseline. *NuSTAR* observation has extended the baseline to 3 more years. The results obtained are well consistent with previous results (Iaria et al., 2018, 2021). The orbital evolution can be explained with the quadratic model with sinusoidal modulation at ~ 24 years with an amplitude of ~ 146 lt-sec. XB 1916–053 shows an orbital period derivative of $\sim 1.5 \times 10^{-11}$ s s⁻¹. The observed period derivative can be interpreted as the mass loss from companion outflowing from the system (Iaria et al., 2021). However, no search for detection of outflow was done in this source as the optical counterpart of XB 1916–053 is dim ($V \sim 21$ mag). Similar to GX 1+4 (Chakrabarty et al., 1998), the P Cygni profile of the He emission line can be studied in XB 1916–053 with sensitive instruments.

5. Conclusion

We have presented a broadband spectral and emission geometry analysis of the XB 1916–053 using simultaneous *Chandra* and *NuSTAR* observations. Our results indicate that most of the emission originates from the NS surface or boundary layer, with a significant fraction undergoing Comptonization by a hot electron cloud, producing the observed hard X-rays. The timing and spectral properties suggest that XB 1916–053 is in a soft state, albeit with a relatively high electron temperature of $kT_e \sim 17$ keV. Additionally, absorption features from highly ionized ions reveal the presence of an accretion disk atmosphere during persistent intervals. While during dipping intervals, the line of sight is obscured by a denser, less ionized outer disk structure or bulge. Furthermore, by analyzing dip arrival times, we have refined the orbital ephemeris of XB 1916–053, extending its baseline by an additional three years.

Declaration of competing interest

The authors declare that they have no known competing financial interests or personal relationships that could have appeared to influence the work reported in this paper.

Acknowledgments

This research has made use of data obtained from the High Energy Astrophysics Science Archive Research Center (HEASARC), provided by NASA's Goddard Space Flight Center. This research has made use of the *NuSTAR* Data Analysis Software (NUSTARDAS) jointly developed by the ASI Science Data Center (ASDC, Italy) and the California Institute of Technology (USA). This research has made use of data obtained from the Chandra Data Archive and software provided by the Chandra X-ray Center (CXC) in the application packages CIAO. The list of Chandra data sets obtained by the Chandra X-ray Observatory is contained in DOI:10.25574/24520. We also thank the anonymous referee for insightful comments and suggestions.

Data availability

The data underlying this article are publicly available in the High Energy Astrophysics Science Archive Research Center (HEASARC) at <https://heasarc.gsfc.nasa.gov/db-perl/W3Browse/w3browse.pl>.

References

- Anitra, A., Di Salvo, T., Iaria, R., Burderi, L., Gambino, A.F., Mazzola, S.M., Marino, A., Sanna, A., Riggio, A., 2021. Spectral analysis of the low-mass X-ray pulsar 4U 1822–371: reflection component in a high-inclination system. *Astron. Astrophys.* 654, A160. <https://doi.org/10.1051/0004-6361/202140557>. arXiv:2109.01023.

- Armas Padilla, M., Ueda, Y., Hori, T., Shidatsu, M., Muñoz-Darias, T., 2017. Suzaku spectroscopy of the neutron star transient 4U 1608-52 during its outburst decay. *Mon. Not. R. Astron. Soc.* 467, 290–297. <https://doi.org/10.1093/mnras/stx020>. arXiv:1701.02728.
- Arnaud, K.A., 1996. XSPEC: the first ten years. In: Jacoby, G.H., Barnes, J. (Eds.), *Astronomical Data Analysis Software and Systems V*, p. 17.
- Bahramian, A., Degenaar, N., 2023. Low-mass X-ray binaries. In: Bambi, Cosimo, Santangelo, Andrea (Eds.), *Handbook of X-Ray and Gamma-Ray Astrophysics*, p. 120.
- Becker, R.H., Smith, B.W., Swank, J.H., Boldt, E.A., Holt, S.S., Pravdo, S.H., Serlemitsos, P.J., 1977. Spectral characteristics of 3U 1915-05, a burst source candidate. *Astrophys. J.* 216, L101–L104. <https://doi.org/10.1086/182520>.
- Beri, A., Sharma, R., Roy, P., Gaur, V., Altamirano, D., Andersson, N., Gittins, F., Celora, T., 2023. AstroSat and NuSTAR observations of XTE J1739-285 during the 2019-2020 outburst. *Mon. Not. R. Astron. Soc.* 521, 5904–5916. <https://doi.org/10.1093/mnras/stad902>. arXiv:2303.13085.
- Bianchi, S., Ponti, G., Muñoz-Darias, T., Petrucci, P.O., 2017. Photoionization instability of the Fe K absorbing plasma in the neutron star transient AX J1745.6-2901. *Mon. Not. R. Astron. Soc.* 472, 2454–2461. <https://doi.org/10.1093/mnras/stx2173>. arXiv:1709.00860.
- Bloser, P.F., Grindlay, J.E., Barret, D., Boirin, L., 2000. RXTE studies of X-ray spectral variations with accretion rate in 4U 1915-05. *Astrophys. J.* 542, 989–999. <https://doi.org/10.1086/317035>. arXiv:astro-ph/0005497.
- Boirin, L., Parmar, A.N., Barret, D., Paltani, S., Grindlay, J.E., 2004. Discovery of X-ray absorption features from the dipping low-mass X-ray binary XB 1916-053 with XMM-Newton. *Astron. Astrophys.* 418, 1061–1072. <https://doi.org/10.1051/0004-6361/20034550>. arXiv:astro-ph/0402294.
- Cackett, E.M., Altamirano, D., Patruno, A., Miller, J.M., Reynolds, M., Linares, M., Wijnands, R., 2009. Broad relativistic iron emission line observed in SAX J1808.4-3658. *Astrophys. J.* 694, L21–L25. <https://doi.org/10.1088/0004-637X/694/1/L21>. arXiv:0901.3142.
- Cash, W., 1979. Parameter estimation in astronomy through application of the likelihood ratio. *Astrophys. J.* 228, 939–947. <https://doi.org/10.1086/156922>.
- Chakrabarty, D., van Kerkwijk, M.H., Larkin, J.E., 1998. Infrared spectroscopy of GX 1+4/V2116 ophiuchi: evidence for a fast red giant wind? *Astrophys. J.* 497, L39–L42. <https://doi.org/10.1086/311271>. arXiv:astro-ph/9802137.
- Chou, Y., Grindlay, J.E., Bloser, P.F., 2001. Timing analysis of the light curve of the dipping-bursting X-ray binary X1916-053. *Astrophys. J.* 549, 1135–1144. <https://doi.org/10.1086/319443>. arXiv:astro-ph/0010465.
- Church, M.J., Dotani, T., Bałucińska-Church, M., Mitsuda, K., Takahashi, T., Inoue, H., Yoshida, K., 1997. Simple photoelectric absorption during dipping in the ASCA observation of XB 1916-053. *Astrophys. J.* 491, 388–394. <https://doi.org/10.1086/304936>. arXiv:astro-ph/9708002.
- Degenaar, N., Miller, J.M., Harrison, F.A., Kennea, J.A., Kouveliotou, C., Younes, G., 2014. High-resolution X-ray spectroscopy of the bursting pulsar GRO J1744-28. *Astrophys. J.* 796, L9. <https://doi.org/10.1088/2041-8205/796/1/L9>. arXiv:1410.4841.
- Díaz Trigo, M., Boirin, L., 2013. Disc atmospheres and winds in X-ray binaries. *Acta Polytech.* 53, 659. arXiv:1210.0318.
- Díaz Trigo, M., Parmar, A.N., Boirin, L., Méndez, M., Kaastra, J.S., 2006. Spectral changes during dipping in low-mass X-ray binaries due to highly-ionized absorbers. *Astron. Astrophys.* 445, 179–195. <https://doi.org/10.1051/0004-6361/20053586>. arXiv:astro-ph/0509342.
- Done, C., Gierliński, M., Kubota, A., 2007. Modelling the behaviour of accretion flows in X-ray binaries. Everything you always wanted to know about accretion but were afraid to ask. *Astron. Astrophys. Rev.* 15, 1–66. <https://doi.org/10.1007/s00159-007-0006-1>. arXiv:0708.0148.
- Frank, J., King, A.R., Lasota, J.P., 1987. The light curves of low-mass X-ray binaries. *Astron. Astrophys.* 178, 137–142.
- Galloway, D.K., Muno, M.P., Hartman, J.M., Psaltis, D., Chakrabarty, D., 2008. Thermonuclear (type I) X-ray bursts observed by the Rossi X-ray timing explorer. *Astrophys. J. Suppl. Ser.* 179, 360–422. <https://doi.org/10.1086/592044>. arXiv:astro-ph/0608259.
- Gambino, A.F., Iaria, R., Di Salvo, T., Del Santo, M., Burderi, L., Matranga, M., Pintore, F., Riggio, A., Sanna, A., 2016. New orbital ephemerides for the dipping source 4U 1323-619: constraining the distance to the source. *Astron. Astrophys.* 589, A34. <https://doi.org/10.1051/0004-6361/201527512>. arXiv:1603.04403.
- Gambino, A.F., Iaria, R., Di Salvo, T., Mazzola, S.M., Marino, A., Burderi, L., Riggio, A., Sanna, A., D'Amico, N., 2019. Spectral analysis of the dipping LMXB system XB 1916-053. *Astron. Astrophys.* 625, A92. <https://doi.org/10.1051/0004-6361/201832984>. arXiv:1904.05770.
- Gladstone, J., Done, C., Gierliński, M., 2007. Analysing the atolls: X-ray spectral transitions of accreting neutron stars. *Mon. Not. R. Astron. Soc.* 378, 13–22. <https://doi.org/10.1111/j.1365-2966.2007.11675.x>. arXiv:astro-ph/0603126.
- Grindlay, J.E., Bailyn, C.D., Cohn, H., Lugger, P.M., Thorstensen, J.R., Wegner, G., 1988. Discovery of a possible X-ray triple: 4U 1915-05. *Astrophys. J.* 334, L25. <https://doi.org/10.1086/185305>.
- Harrison, F.A., Craig, W.W., Christensen, F.E., Hailey, C.J., Zhang, W.W., Boggs, S.E., Stern, D., Cook, W.R., Forster, K., Giommi, P., Grefenstette, B.W., Kim, Y., Kitaguchi, T., Koglin, J.E., Madsen, K.K., Mao, P.H., Miyasaka, H., Mori, K., Perri, M., Pivovarov, M.J., Puccetti, S., Rana, V.R., Westergaard, N.J., Willis, J., Zoglauer, A., An, H., Bachetti, M., Barrière, N.M., Bellm, E.C., Bhalerao, V., Brejnholt, N.F., Fuerst, F., Liebe, C.C., Markwardt, C.B., Nynka, M., Vogel, J.K., Walton, D.J., Wik, D.R., Alexander, D.M., Cominsky, L.R., Hornschemeier, A.E., Hornstrup, A., Kaspi, V.M., Madejski, G.M., Matt, G., Molendi, S., Smith, D.M., Tomsick, J.A., Ajello, M., Ballantyne, D.R., Baloković, M., Barret, D., Bauer, F.E., Blandford, R.D., Brandt, W.N., Brenneman, L.W., Chiang, J., Chakrabarty, D., Chenevez, J., Comastri, A., Dufour, F., Elvis, M., Fabian, A.C., Farrah, D., Fryer, C.L., Gotthelf, E.V., Grindlay, J.E., Helfand, D.J., Krivonoz, R., Meier, D.L., Miller, J.M., Natalucci, L., Ogle, P., Ofek, E.O., Ptak, A., Reynolds, S.P., Rigby, J.R., Tagliaferri, G., Thorsett, S.E., Treister, E., Urry, C.M., 2013. The nuclear spectroscopic telescope array (NuSTAR) high-energy X-ray mission. *Astrophys. J.* 770, 103. <https://doi.org/10.1088/0004-637X/770/2/103>. arXiv:1301.7307.
- Hasinger, G., van der Klis, M., 1989. Two patterns of correlated X-ray timing and spectral behaviour in low-mass X-ray binaries. *Astron. Astrophys.* 225, 79–96.
- Hu, C.P., Chou, Y., Chung, Y.Y., 2008. A parameterization study of the properties of the X-ray dips in the low-mass X-ray binary X1916-053. *Astrophys. J.* 680, 1405–1411. <https://doi.org/10.1086/527549>. arXiv:0712.1868.
- Hyodo, Y., Ueda, Y., Yuasa, T., Maeda, Y., Makishima, K., Koyama, K., 2009. Timing and spectral study of AXJ1745.6-2901 with Suzaku. *Publ. Astron. Soc. Jpn.* 61, S99–S106. <https://doi.org/10.1093/pasj/61.sp1.S99>.
- Iaria, R., Di Salvo, T., Lavagetto, G., Robba, N.R., Burderi, L., 2006. Chandra observation of the persistent emission from the dipping source XB 1916-053. *Astrophys. J.* 647, 1341–1348. <https://doi.org/10.1086/505616>. arXiv:astro-ph/0605055.
- Iaria, R., Di Salvo, T., Gambino, A.F., Del Santo, M., Romano, P., Matranga, M., Galiano, C.G., Scarano, F., Riggio, A., Sanna, A., Pintore, F., Burderi, L., 2015. Signature of the presence of a third body orbiting around XB 1916-053. *Astron. Astrophys.* 582, A32. <https://doi.org/10.1051/0004-6361/201526500>. arXiv:1507.08108.
- Iaria, R., Gambino, A.F., Di Salvo, T., Burderi, L., Matranga, M., Riggio, A., Sanna, A., Scarano, F., D'Ai, A., 2018. A possible solution of the puzzling variation of the orbital period of MXB 1659-298. *Mon. Not. R. Astron. Soc.* 473, 3490–3499. <https://doi.org/10.1093/mnras/stx2529>. arXiv:1703.05294.
- Iaria, R., Sanna, A., Di Salvo, T., Gambino, A.F., Mazzola, S.M., Riggio, A., Marino, A., Burderi, L., 2021. Evidence of a non-conservative mass transfer in the ultra-compact X-ray source XB 1916-053. *Astron. Astrophys.* 646, A120. <https://doi.org/10.1051/0004-6361/202039225>. arXiv:2012.08826.
- Iaria, R., Di Salvo, T., Anitra, A., Miceli, C., Barra, F., Leone, W., Burderi, L., Sanna, A., Riggio, A., 2024. Confirmation of the presence of a CRSF in the NICER spectrum of X 1822-371. *Astron. Astrophys.* 683, A79. <https://doi.org/10.1051/0004-6361/202345888>. arXiv:2401.03698.
- Ibragimov, A., Poutanen, J., 2009. Accreting millisecond pulsar SAX J1808.4-3658 during its 2002 outburst: evidence for a receding disc. *Mon. Not. R. Astron. Soc.* 400, 492–508. <https://doi.org/10.1111/j.1365-2966.2009.15477.x>. arXiv:0901.0073.
- Jain, C., Paul, B., Sharma, R., Jaleel, A., Dutta, A., 2017. Indication of a massive circumbinary planet orbiting the low-mass X-ray binary MXB 1658-298. *Mon. Not. R. Astron. Soc.* 468, L118–L122. <https://doi.org/10.1093/mnras/513.1/118>. arXiv:1703.04433.
- Jain, C., Sharma, R., Paul, B., 2022. Eclipse timings of the LMXB XTE J1710-281: discovery of a third orbital period glitch. *Mon. Not. R. Astron. Soc.* 517, 2131–2137. <https://doi.org/10.1093/mnras/stac2804>. arXiv:2209.13406.
- Juett, A.M., Chakrabarty, D., 2006. Detection of highly ionized metal absorption lines in the ultracompact X-ray dipper 4U 1916-05. *Astrophys. J.* 646, 493–498. <https://doi.org/10.1086/504863>. arXiv:astro-ph/0604046.
- Kaastra, J.S., Bleeker, J.A.M., 2016. Optimal binning of X-ray spectra and response matrix design. *Astron. Astrophys.* 587, A151. <https://doi.org/10.1051/0004-6361/201527395>. arXiv:1601.05309.
- Kluźniak, W., Rappaport, S., 2007. Magnetically torqued thin accretion disks. *Astrophys. J.* 671, 1990–2005. <https://doi.org/10.1086/522954>. arXiv:0709.2361.
- Kubota, A., Tanaka, Y., Makishima, K., Ueda, Y., Dotani, T., Inoue, H., Yamaoka, K., 1998. Evidence for a black hole in the X-ray transient GRS 1009-45. *Publ. Astron. Soc. Jpn.* 50, 667–673. <https://doi.org/10.1093/pasj/50.6.667>.
- Lewin, W.H.G., van der Klis, M., 2006. *Compact Stellar X-Ray Sources*. Cambridge University Press.
- Lin, D., Remillard, R.A., Homan, J., 2007. Evaluating spectral models and the X-ray states of neutron star X-ray transients. *Astrophys. J.* 667, 1073–1086. <https://doi.org/10.1086/521181>. arXiv:astro-ph/0702089.
- Lin, D., Remillard, R.A., Homan, J., 2009. Spectral states of XTE J1701 - 462: link between Z and Atoll sources. *Astrophys. J.* 696, 1257–1277. <https://doi.org/10.1088/0004-637X/696/2/1257>. arXiv:0901.0031.
- Long, M., Romanova, M.M., Lovelace, R.V.E., 2005. Locking of the rotation of disk-accreting magnetized stars. *Astrophys. J.* 634, 1214–1222. <https://doi.org/10.1086/497000>. arXiv:astro-ph/0510659.
- Ludlam, R.M., Miller, J.M., Degenaar, N., Sanna, A., Cackett, E.M., Altamirano, D., King, A.L., 2017. Truncation of the accretion disk at one-third of the Eddington limit in the neutron star low-mass X-ray binary aquila X-1. *Astrophys. J.* 847, 135. <https://doi.org/10.3847/1538-4357/aa8b1b>. arXiv:1709.01559.
- Marino, A., Anitra, A., Mazzola, S.M., Di Salvo, T., Sanna, A., Bult, P., Guillot, S., Mancuso, G., Ng, M., Riggio, A., Albayati, A.C., Altamirano, D., Arzoumanian, Z., Burderi, L., Cabras, C., Chakrabarty, D., Deioiso, N., Gendreau, K.C., Iaria, R., Manca, A., Strohmayer, T.E., 2022. Outflows and spectral evolution in the eclipsing AMXP SWIFT J1749.4-2807 with NICER, XMM-Newton, and NuSTAR. *Mon. Not. R. Astron. Soc.* 515, 3838–3852. <https://doi.org/10.1093/mnras/stac2038>. arXiv:2207.08637.
- Mitsuda, K., Inoue, H., Koyama, K., Makishima, K., Matsuoka, M., Ogawara, Y., Suzuki, K., Tanaka, Y., Shibazaki, N., Hirano, T., 1984. Energy spectra of low-mass binary X-ray sources observed from TENMA. *Publ. Astron. Soc. Jpn.* 36, 741–759.

- Mukherjee, D., Bult, P., van der Klis, M., Bhattacharya, D., 2015. The magnetic-field strengths of accreting millisecond pulsars. *Mon. Not. R. Astron. Soc.* 452, 3994–4012. <https://doi.org/10.1093/mnras/stv1542>. arXiv:1507.02138.
- Muñoz-Darias, T., Fender, R.P., Motta, S.E., Belloni, T.M., 2014. Black hole-like hysteresis and accretion states in neutron star low-mass X-ray binaries. *Mon. Not. R. Astron. Soc.* 443, 3270–3283. <https://doi.org/10.1093/mnras/stu1334>. arXiv:1407.1318.
- Ponti, G., Muñoz-Darias, T., Fender, R.P., 2014. A connection between accretion state and Fe K absorption in an accreting neutron star: black hole-like soft-state winds? *Mon. Not. R. Astron. Soc.* 444, 1829–1834. <https://doi.org/10.1093/mnras/stu1742>. arXiv:1407.4468.
- Ponti, G., Bianchi, S., Muñoz-Darias, T., De Marco, B., Dwelly, T., Fender, R.P., Nandra, K., Rea, N., Mori, K., Haggard, D., Heinke, C.O., Degenaar, N., Aramaki, T., Clavel, M., Goldwurm, A., Hailey, C.J., Israel, G.L., Morris, M.R., Rushton, A., Terrier, R., 2015. On the Fe K absorption - accretion state connection in the Galactic Centre neutron star X-ray binary AX J1745.6-2901. *Mon. Not. R. Astron. Soc.* 446, 1536–1550. <https://doi.org/10.1093/mnras/stu1853>. arXiv:1409.3224.
- Ponti, G., De, K., Muñoz-Darias, T., Stella, L., Nandra, K., 2017. The puzzling orbital period evolution of the LMXB AX J1745.6-2901. *Mon. Not. R. Astron. Soc.* 464, 840–849. <https://doi.org/10.1093/mnras/stw2317>. arXiv:1511.02855.
- Ponti, G., Bianchi, S., De Marco, B., Bahramian, A., Degenaar, N., Heinke, C.O., 2019. Evolution of the disc atmosphere in the X-ray binary MXB 1659-298, during its 2015-17 outburst. *Mon. Not. R. Astron. Soc.* 487, 858–870. <https://doi.org/10.1093/mnras/stz1245>. arXiv:1905.01308.
- Popham, R., Sunyaev, R., 2001. Accretion disk boundary layers around neutron stars: X-ray production in low-mass X-ray binaries. *Astrophys. J.* 547, 355–383. <https://doi.org/10.1086/318336>. arXiv:astro-ph/0004017.
- Psaltis, D., Chakrabarty, D., 1999. The disk-magnetosphere interaction in the accretion-powered millisecond pulsar SAX J1808.4-3658. *Astrophys. J.* 521, 332–340. <https://doi.org/10.1086/307525>. arXiv:astro-ph/9809335.
- Raman, G., Maitra, C., Paul, B., 2018. Observation of variable pre-eclipse dips and disc winds in the eclipsing LMXB XTE J1710-281. *Mon. Not. R. Astron. Soc.* 477, 5358–5366. <https://doi.org/10.1093/mnras/sty918>. arXiv:1804.06073.
- Reeves, J., Done, C., Pounds, K., Terashima, Y., Hayashida, K., Anabuki, N., Uchino, M., Turner, M., 2008. On why the iron K-shell absorption in AGN is not a signature of the local warm/hot intergalactic medium. *Mon. Not. R. Astron. Soc.* 385, L108–L112. <https://doi.org/10.1111/j.1745-3933.2008.00443.x>. arXiv:0801.1587.
- Retter, A., Chou, Y., Bedding, T.R., Naylor, T., 2002. Detection of negative superhumps in a low-mass X-ray binary - an end to the long debate on the nature of V1405 Aql (X1916-053). *Mon. Not. R. Astron. Soc.* 330, L37–L42. <https://doi.org/10.1046/j.1365-8711.2002.05280.x>. arXiv:astro-ph/0112542.
- Sakurai, S., Yamada, S., Torii, S., Noda, H., Nakazawa, K., Makishima, K., Takahashi, H., 2012. Accretion geometry of the low-mass X-ray binary aquila X-1 in the soft and hard states. *Publ. Astron. Soc. Jpn.* 64, 72. <https://doi.org/10.1093/pasj/64.4.72>. arXiv:1201.5891.
- Sharma, P., Sharma, R., Jain, C., Dutta, A., 2020a. Broad-band spectral analysis of LMXB XTE J1710-281 with Suzaku. *Mon. Not. R. Astron. Soc.* 496, 197–205. <https://doi.org/10.1093/mnras/staa1516>. arXiv:2006.03291.
- Sharma, R., Jaleel, A., Jain, C., Pandey, J.C., Paul, B., Dutta, A., 2018. Spectral properties of MXB 1658-298 in the low/hard and high/soft state. *Mon. Not. R. Astron. Soc.* 481, 5560–5569. <https://doi.org/10.1093/mnras/sty2678>. arXiv:1810.01827.
- Sharma, R., Jain, C., Dutta, A., 2019. Study of the reflection spectra of SAX J1748.9-2021. *Mon. Not. R. Astron. Soc.* 482, 1634–1639. <https://doi.org/10.1093/mnras/sty2808>. arXiv:1810.07115.
- Sharma, R., Beri, A., Sanna, A., Dutta, A., 2020b. A broad-band look of the accreting millisecond X-ray pulsar SAX J1748.9-2021 using AstroSat and XMM-Newton. *Mon. Not. R. Astron. Soc.* 492, 4361–4368. <https://doi.org/10.1093/mnras/staa109>. arXiv:2001.03594.
- Shimura, T., Takahara, F., 1995. On the spectral hardening factor of the X-ray emission from accretion disks in black hole candidates. *Astrophys. J.* 445, 780. <https://doi.org/10.1086/175740>.
- Sidoli, L., Oosterbroek, T., Parmar, A.N., Lumb, D., Erd, C., 2001. An XMM-Newton study of the X-ray binary MXB 1659-298 and the discovery of narrow X-ray absorption lines. *Astron. Astrophys.* 379, 540–550. <https://doi.org/10.1051/0004-6361:20011322>. arXiv:astro-ph/0109417.
- Sidoli, L., Parmar, A.N., Oosterbroek, T., Lumb, D., 2002. Discovery of complex narrow X-ray absorption features from the low-mass X-ray binary GX 13+1 with XMM-Newton. *Astron. Astrophys.* 385, 940–946. <https://doi.org/10.1051/0004-6361:20020192>. arXiv:astro-ph/0202077.
- Smale, A.P., Mason, K.O., White, N.E., Gottwald, M., 1988. X-ray observations of the 50-min dipping source XB 1916-053. *Mon. Not. R. Astron. Soc.* 232, 647–660. <https://doi.org/10.1093/mnras/232.3.647>.
- Smale, A.P., Mason, K.O., Williams, O.R., Watson, M.G., 1989. GINGA observations of the dipping X-ray binary XB 1916-053. *Publ. Astron. Soc. Jpn.* 41, 607–615.
- Trueba, N., Miller, J.M., Fabian, A.C., Kaastra, J., Kallman, T., Lohfink, A., Proga, D., Raymond, J., Reynolds, C., Reynolds, M., Zoghbi, A., 2020. A redshifted inner disk atmosphere and transient absorbers in the ultracompact neutron star X-ray binary 4U 1916-053. *Astrophys. J.* 899, L16. <https://doi.org/10.3847/2041-8213/aba9de>. arXiv:2008.01083.
- van der Klis, M., 2006. A review of rapid X-ray variability in X-ray binaries. In: Lewin, W., van der Klis, M. (Eds.), *Compact Stellar X-Ray Sources*, p. 39. arXiv:astro-ph/0410551.
- Verner, D.A., Ferland, G.J., Korista, K.T., Yakovlev, D.G., 1996. Atomic data for astrophysics. II. New analytic FITS for photoionization cross sections of atoms and ions. *Astrophys. J.* 465, 487. <https://doi.org/10.1086/177435>. arXiv:astro-ph/9601009.
- Walter, F.M., Mason, K.O., Clarke, J.T., Halpern, J., Grindlay, J.E., Bowyer, S., Henry, J.P., 1982. Discovery of a 50 MN binary period and a likely 22 magnitude optical counterpart for the X-ray burster 4U 1915-05. *Astrophys. J.* 253, L67–L71. <https://doi.org/10.1086/183738>.
- White, N.E., 1989. X-ray binaries. *Astron. Astrophys. Rev.* 1, 85–110. <https://doi.org/10.1007/BF00872485>.
- White, N.E., Swank, J.H., 1982. The periodic absorption events from 4U 1915-05. *Astrophys. J.* 253, L61–L66. <https://doi.org/10.1086/183737>.
- Wilms, J., Allen, A., McCray, R., 2000. On the absorption of X-rays in the interstellar medium. *Astrophys. J.* 542, 914–924. <https://doi.org/10.1086/317016>. arXiv:astro-ph/0008425.
- Zdziarski, A.A., Szanecki, M., Poutanen, J., Gierliński, M., Biernacki, P., 2020. Spectral and temporal properties of Compton scattering by mildly relativistic thermal electrons. *Mon. Not. R. Astron. Soc.* 492, 5234–5246. <https://doi.org/10.1093/mnras/staa159>. arXiv:1910.04535.
- Zhang, Z., Makishima, K., Sakurai, S., Sasano, M., Ono, K., 2014. Probing the accretion scheme of the dipping X-ray binary 4U 1915-05 with Suzaku. *Publ. Astron. Soc. Jpn.* 66, 120. <https://doi.org/10.1093/pasj/psu117>. arXiv:1409.2091.
- Zhang, Z., Sakurai, S., Makishima, K., Nakazawa, K., Ono, K., Yamada, S., Xu, H., 2016. Suzaku observation of the high-inclination binary EXO 0748-676 in the hard state. *Astrophys. J.* 823, 131. <https://doi.org/10.3847/0004-637X/823/2/131>. arXiv:1603.05913.